INVESTIGATIONS ON THE DYNAMIC COEFFICIENTS OF IMPELLER EYE LABYRINTH SEALS

by

Norbert G. Wagner

Head of Component Development

Klaus Steff

Manager of Development Mechanics

Rainer Gausmann

Development Engineer

and

Marcus Schmidt

Development Engineer

Siemens Energy Sector, Oil & Gas Division

Duisburg, Germany

Norbert G. Wagner is Head of Component Development within Siemens Energy Sector, Oil and Gas Division, Compressor Product Development, in Duisburg, Germany. In this capacity, he is responsible for basic technologies. During his more than 25 years with this company, Dr. Wagner has given special attention to rotordynamics of high-pressure applications and to active magnetic bearings. He has conducted extensive analytical and experimental investigations on the effect of labyrinth seals on rotor stability and he has authored several papers on this issue.

Dr. Wagner received his Diplom degree from the University of Duisburg (1981) and his doctorate from the Technical University of Darmstadt (2000).

Klaus Steff is Manager of Development Mechanics and principal mechanics/ dynamics expert within the Siemens Energy Sector, Oil and Gas Division, Compressor Product Development, in Duisburg, Germany. Working for more than 20 years with this company, he has covered a wide range of experimental and analytical investigations on rotordynamics, bearings, structural dynamics, and software development. He is active in several research committees: FVV, FVA, TRC, and Romac, and has coauthored several papers on rotor stability.

Mr. Steff received his Diplom degree from the University of Duisburg (1987).

Rainer Gausmann is a Development Engineer within the Siemens Energy Sector, Oil and Gas Division, Compressor Product Development, in Duisburg, Germany. His main scope of activity is the rotordynamics of motors and compressors levitated by active magnetic bearings. Special focus within his research activities is the stability of these rotors in higher pressure applications. This is directly linked to the activities on Siemens in-house seal test rig with focus on the identification of the seal characteristics.

Dr. Gausmann received his Diplom degree from the University of Hannover (1997) and his doctorate from Technical University of Karlsruhe (2005).

Marcus Schmidt is a Development Engineer within the Siemens Energy Sector, Oil and Gas Division, Compressor Product Development, in Duisburg, Germany. After five years in the design development department for centrifugal compressors, he moved into the development mechanics department in 2004. In his current capacity, he works in the field of rotordynamics with special focus on experimental investigations on the effect of labyrinth seals on rotor stability.

Mr. Schmidt received his Diplom degree (1999) from the University of Duisburg.

ABSTRACT

For many application fields of turbocompressors the rotor stability has become the most important part of the rotordynamic analysis. A comprehensive knowledge of these seal forces is mandatory to ensure an adequate overall design of the compressor as early as the quotation phase. While in earlier times the focus was on the balance drum contribution as the major source of excitation, it has in the meantime become evident that the effects from the impeller eye-seals also have to be considered as a further destabilizing contribution. However, up to now the task of measurement of impeller-eye-seal dynamic coefficients has remained a major challenge.

This paper presents a new approach for generation of high-quality data on a unique full-scale high-pressure test rig, in which specific attention is paid to impeller-eye seals. The applied strategy combines results from the test rig obtained from different methods with findings from computational fluid dynamic (CFD) investigations.

The publication of dimensional data offers further use of these results within the turbomachinery community.

INTRODUCTION

In the mid-seventies the instabilities of the Kaybob (Smith, 1974) and Ekofisk (Cochrane, 1976) compressors erased the former belief that the gas-seal forces are negligible quantities. More than 30 years of research and development have taken place since then, but a reliable determination of these destabilizing forces seems to be still an issue of highest interest, as outlined below. This high importance is also driven by the continuously changing requirements on centrifugal compressor duties.

As oil fields deplete in the accessible regions of the world, oil companies are forced to search for oil in fields located in increasingly difficult environments, at increasing depth below ground, and increasing remoteness from the markets. Frequently this remoteness leads to liquefaction of huge amounts of natural gas in large liquefied natural gas (LNG) plants; this is one of the currently booming markets.

In other cases it is necessary to reinject gas into the oil reservoir, where the trend is toward higher well-head pressures. This is not only to boost oil field production; more and more of the new fields have a less favorable gas composition, e.g., with extremely high H_2S content. In such cases reinjection is also driven by ecological considerations. These are also the key driver for other emerging markets such as CO_2 compression. There are various ways of processing this greenhouse gas, ranging from enhanced oil recovery (EOR) via CO_2 sequestration into underground storage to transportation, in particular from fossil power plants through dedicated pipelines.

In these markets, which are currently highlighted, dynamic seal forces play a decisive role in rotordynamics and consequently in the overall compressor design. Beyond these applications there are many other compressors, in which competition between vendors leads to a removal of too large safety margins and which requires accurate knowledge of the dynamic seal forces. In any case, an inaccurate prediction may result in unstable, excessive vibrations during shop-testing or—even worse—during commissioning of the unit or they may also appear later in the production phase. The ongoing trend for expanded size and power rating of projects leads to an increasing commercial risk of late delivery or downtime.

The latest edition of API 617 (2002) now accounts for the relevance of the dynamic seal forces and asks explicitly for a stability analysis. Since there is no generally accepted method for determination of the dynamic seal forces, very different approaches are in use and lead to a very wide spread of rotor stability results. This has been demonstrated most impressively in a recent paper of Kocur, et al. (2007), in which the result of a comprehensive survey on tilting-pad journal-bearing and gas-labyrinth seal coefficients is published. For a complete set of given input data respondents from academia, manufacturers, users, and consultants provided their dynamic coefficients for bearings and seals, which were then applied to the given model rotor. Frequency predictions for the first forward mode ranged from 6000 to 11,300 cpm. Logarithmic decrement magnitudes ranged from +1.0 to−1.0 even after ignoring the extremes!

While the bearing data, of course, play one major role in these variations, this paper will focus on the dynamic-seal coefficients and their contribution to rotordynamics. The impeller-eye seals, for which no high-quality test data were published yet, are addressed specifically.

The initial comprehensive measurements of cross-coupled stiffness made by Benckert (1980) were related to relatively long labyrinth seals used on balance drums. It rapidly became clear that, in addition to the destabilizing cross-coupled stiffness, damping forces would also necessarily be present and that the impeller-eye seals would likewise need to be considered (Kirk, 1988). Comprehensive and systematic experiments on component level with measurement of all stiffness and damping coefficients were conducted at a major Texas university, e.g., Childs and Scharrer (1986) to Childs and Picardo (2005), and by Wagner and Steff (1996) and Wagner (2001).

An interesting approach of comparing CFD results with cavity-pressure measurements was presented by Schettel, et al. (2005). Although a turbine-style comb-groove seal with two cavities was tested only with a static eccentricity rather than a whirling rotor and this at relatively low parameters, the evaluation of the circumferential pressure distribution gave interesting insights. In contradiction to Benckert's statements, radial as well as axial pressure profiles were established, influencing the force prediction from these pressure measurements. Further analysis revealed a large dependency of the direct stiffness coefficient on the test procedure "pressure," "stator force," and "rotor force." They also point to the impact of the flow upstream and downstream of the seal on the seal dynamic coefficients.

Although there are a number of agreements on some fundamental aspects like the strong influence of the inlet swirl and the effectiveness of swirl brakes, there are still a lot of disputes and contradictions about the dynamic seal coefficients. Just a few examples might give an idea about the uncertainties involved in addition to the contradictions as stated in the book of Childs (1993). An excellent and even more actual survey was given by Childs and Vance (2007).

Baumann (1999) has checked the accuracy of the dynamic labyrinth coefficients, which have been calculated by using a finite-differences method, by means of natural-frequency and damping measurements. It was not possible to explain all of the observed phenomena, even though the calculated values were adapted to the measured values by reversing the sign for the calculated direct stiffness and by doubling all of the other stiffness and damping coefficients.

According to Memmott (1999) consideration of the damping of impeller-eye seals leads to unduly favorable stability results. In this paper a negative direct stiffness of toothed labyrinths is being disregarded, since this could not be confirmed by measurement of the natural-frequency on compressor rotors.

In an attempt to further refine the overall rotordynamic model, Moore, et al. (2007), have predicted dynamic coefficients of a centrifugal impeller by means of CFD, while using a bulk-flow model only for the labyrinth seals. In this study only the CFD results for the cross-coupled stiffness are included for a direct comparison to the other empirical methods. If the CFD-predicted damping terms are included, the resulting aero cross-coupling will be decreased, possibly to a point below the stability threshold (i.e., instability not predicted in contrast to the experience from a machine in the field). This work contributes to the ongoing debate on the significance of such dynamic impeller forces. At the end of the present paper a contribution to this issue is also provided.

Another paper also considers such dynamic coefficients of a centrifugal impeller, but in this paper of Gupta, et al. (2007), a bulk-flow model is employed for prediction of these impeller coefficients. The compressor under investigation is equipped with a hole-pattern seal, which dominates the entire vibration behavior of this compressor. Therefore the authors have some reservations regarding the impeller-coefficient validation, since a very small quantity was validated out of an overall system behavior, in which the uncertainty of the dominant element (hole-pattern seal) is most likely larger than the quantity of the effect of interest (impeller coefficients).

From the bearing and seal coefficient survey as published by Kocur, et al. (2007), the authors feel some endorsement for their reservations that the uncertainty of the first-order effects (oil bearings, balance drum labyrinth, and hole-pattern seal coefficients) needs to be improved first, before a calibration of smaller, higher-order effects (impeller coefficients) can be based on these first-order effect (bearing and balance drum seal coefficients) predictions.

Some years ago it was decided to revamp the existing test facility for reasons as outlined in the next chapter and to support and substantiate these experimental data in a further step by numerical analyses (CFD).

A survey on this research effort is given and some results were provided, which might form a contribution to a "gold standard" as proposed by Kocur, et al. (2007). Since the biggest lack in published data relates to impeller-eye seals, they were selected in this paper from the comprehensive in-house research project.

ROTORDYNAMICS DESIGN STRATEGY

With the importance of the rotor stability in mind, several approaches are feasible design strategies. One design strategy could be to extend the allowable application range of a compressor empirically, until the stability threshold is reached. Another strategy could be to rely only on the most complex numerical models for bearings and seals, tempted by the ever-increasing computer power.

It is the authors' firm belief that the best results in terms of reliability of the analysis can be obtained only by systematic analyses on a component level, which should be conducted with state-of-the-art numerical tools and be anchored in high quality experiments on the component. The better the understanding of the physics involved, the more reliable are the results of the developed models. This understanding must include a serious examination of uncertainties involved (from fabrication of parts up to measurement), parameter sensitivities, boundary conditions, and a careful validation of the data obtained.

This is in contrast to the application of simple empirical formulae in the design process, like the Wachel number of Wachel and von Nimitz (1980) and similar correlations. They are very easy to apply, but they do not consider the important design details and thus are suitable for an initial screening of designs only. Similarly it is not recommended to just try another software package, without questioning and understanding its background and validation.

The bearing characteristics are of the highest importance for any rotordynamic analysis, since they form the baseline characteristics of the entire rotordynamic system. While this is done in separate projects, this paper focuses on the seal forces.

For achievement of high-quality data on a component level the authors' company decided to develop and put into operation a dedicated component tester. The methodology and some results of the seal test rig have been reported by Wagner and Steff (1996).

Although the results from this test rig have now been applied for more than a decade with great success—not a single case of rotor instability has been observed since—it was decided to further improve the quality of the results and to expand the capabilities of this tester. Details are given in the next section.

A major addition to the previous test program was the deployment of CFD for better understanding of the test results. This approach provides several advantages:

- Better understanding and improved interpretation of the test results
- Check for consistency of trends from experiment and numerical simulation.
- Calibrate CFD on the experimental database.
- Use CFD as a calibrated tool for extrapolations, where testing is infeasible or uneconomic.
- Anchor the (simplified) engineering tool (in-house software package) for the designers' day-to-day rotordynamic work on these CFD extrapolations, which are in turn calibrated and consistency-checked with the experimental database.

This strategy provides reliable and high-quality results. It is very economical in the application of the derived engineering tool software, because for the high project count that has to be processed each day, CFD is not (yet) a suitable tool for all the required variations.

The last—but not least—element in this design strategy is the validation of the rotordynamic design on real compressors. One option is testing of the stability threshold by careful approach of this limit during full-load test; another option is application of a magnetic shaker onto a shaft extension, which allows for natural frequency and logarithmic decrement determination of this modified arrangement during load testing and comparison with analytical results for this modified condition.

FUNDAMENTAL CONSIDERATIONS FOR SEAL FORCE DETERMINATION

Both experimental and numerical determination methods of impeller-eye seal forces have the commonality of lacking "true" values for benchmarking purposes. The only "true data" comes from production machines. However, due to all the uncertainties involved in a production machine, from manufacturing and alignment tolerances, bearing characteristic uncertainties, and a multiplicity of seal locations, it seems not reasonable to try to extract single-component dynamic data from overall system measurements.

Since both experimental and numerical determination methods unavoidably deal with uncertainties, researchers have been looking desperately for reference data of the highest quality, in particular for impeller-eye seals, where the dynamic coefficients are of relatively small order of magnitude only in the existent test rigs.

Numerical analyses fall either into the category of bulk-flow models or of computational fluid dynamics with high resolution grids to resolve the fundamental equations of mass, momentum, and energy. While the bulk-flow models are quite simplified and can provide reliable data only if anchored to experimental data, CFD is currently state-of-the-art. However, it is still quite time-consuming and requires proper consideration of the boundary conditions, the definition of the analyzed flow domain including the rotor/stator interface.

As will be shown later in the paper, a number of uncertainties can be eliminated by means of comprehensive studies. Nevertheless, even after establishment and application of best practice guidelines, the need for benchmarking data persists.

All experimental methods suffer—more or less—difficulties in simulation of realistic operating conditions, test of non-ideal geometries, most demanding calibration needs with limitations in transducers and instrumentations and unavoidable disturbances, which make it really challenging to isolate the "true" effect. Therefore, high-quality reference data are also highly desired for the experimenters.

Combined Experimental/Numerical Effort

The above-mentioned difficulties clearly call for a combined experimental/numerical effort, being the focus of this paper. Utmost efforts are needed for both categories of work in order to minimize the uncertainties involved.

The results from the conducted numerical and experimental analyses should not only be compared in terms of some stiffness and damping coefficients. The quality of the force models needs to be evaluated and conclusions derived from one method should be investigated in the other method as well.

Further, it would be most beneficial and valuable to obtain and compare intermediate results, like dynamic pressures in the labyrinth cavities. With such intermediate results, differences between measurement and calculation could be tracked down and provide a basis for improvements of the chosen method.

Another piece of the puzzle that could be utilized is the analysis of the overall system dynamics. While it has been outlined before, that this kind of analysis of full-size production machines cannot be recommended for parameter extraction, it is well worthwhile to analyze the overall system dynamics of the entire seal-test rig. In particular it is possible to generate a very detailed model of the complete magnetic bearing system and of the rotor to identify the dynamic seal coefficients from excitation of the rotor over a very wide frequency range. This approach of a combined experimental/numerical effort is also illustrated in Figure 1.

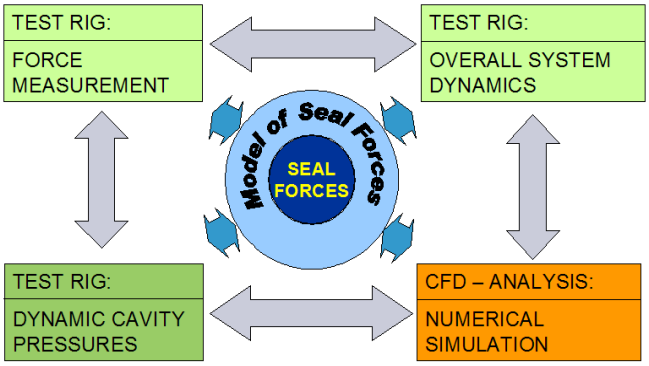

Figure 1. Sketch of Combined Experimental/Numerical Effort for Determination of Seal Forces.

Models for Approximation of Test Results

The circles in the center of Figure 1 shall pronounce that different mathematical models may be used in order to reflect the "true" nature of the seal forces. A general mathematical model of frequency-dependant transfer functions for the direct seal forces D(s) and cross-coupled seal forces E(s) in the Laplace domain is given by:

$$-\begin{pmatrix} F_x \\ F_y \end{pmatrix} = \begin{bmatrix} D(s) & E(s) \\ -E(s) & D(s) \end{bmatrix} \cdot \begin{pmatrix} x \\ y \end{pmatrix} \tag{1}$$

Equation (1) uses only the quite common assumption of a motion around the seal center, resulting in this skew symmetric matrix. General transfer functions D(s) and E(s) can be determined by measurement of the seal forces for circular forward and backward motions. This capability is important for analysis of damper seals, which exhibit nonlinear frequency-dependant characteristics. For a forward respectively backward motion (denoted by an index + respectively −), the radial (F_r) and tangential forces (F_t) can be rewritten to:

$$\begin{aligned} -F_{r+}/e &= \Re(D) + \Im(E) \\ -F_{r-}/e &= \Re(D) - \Im(E) \\ -F_{t+}/e &= -\Re(E) + \Im(D) \\ -F_{t-}/e &= -\Re(E) - \Im(D) \end{aligned} \tag{2}$$

with the use of *e* as orbit radius. The operators $\Re(G(s))$, $\Im(G(S))$ in Equation (2) refer to the real and imaginary part of a complex transfer function G(s), respectively.

For the impeller-eye labyrinths, which are the focus of this paper, this general format is not needed. However, examination of the results for positive and backward motion indicates clearly that the classical stiffness and damping model with direct and cross-coupled coefficients is an inadequate model. Therefore, the linear model for the transfer functions D and E as described in Schmied, et al. (2002), is expanded to fit the measured forces also by inertia terms m_R and m_Q in the following way:

$$\begin{aligned} D(j\Omega) &= k_R + j\Omega\, d_R - \Omega^2 m_R \\ E(j\Omega) &= k_Q + j\Omega\, d_Q - \Omega^2 m_Q \end{aligned} \tag{3}$$

This results in the radial and tangential forces over the orbit radius e:

$$\begin{aligned} -\frac{F_{r\pm}}{e} &= \Re(D) \pm \Im(E) = k_R \pm \Omega\, d_Q - \Omega^2 m_R \\ -\frac{F_{t\pm}}{e} &= -\Re(E) \pm \Im(D) = -k_Q \pm \Omega\, d_R + \Omega^2 m_Q \end{aligned} \tag{4}$$

for forward (+) and backward (−) motion. Index "R" always indicates the direct terms on the stiffness, damping, and inertia matrices main diagonal, while index "Q" indicates cross-coupled terms on the secondary diagonal of the matrices. For rotordynamic purposes the coefficients of Equation (4) are used in this way:

$$\begin{bmatrix} -F_x \\ -F_y \end{bmatrix} = \begin{bmatrix} k_R & k_Q \\ -k_Q & k_R \end{bmatrix} \begin{bmatrix} x \\ y \end{bmatrix} + \begin{bmatrix} d_R & d_Q \\ -d_Q & d_R \end{bmatrix} \begin{bmatrix} \dot{x} \\ \dot{y} \end{bmatrix} + \begin{bmatrix} m_R & m_Q \\ -m_Q & m_R \end{bmatrix} \begin{bmatrix} \ddot{x} \\ \ddot{y} \end{bmatrix} \tag{5}$$

In case the inertia terms m_R and m_Q are determined to be zero, this model reduces to the well-known spring/damper model. At this point it shall be noted that many rotordynamic codes are unable to handle these inertia terms and consider stiffness and damping only.

In some cases engineers were puzzled about the sign of the direct stiffness coefficient. This may be caused by an inadequate model, trying to make a linear fit to a quadratic curve. As shown as an example in Figure 2, accidental stiffness and damping numbers may be obtained when fitting a straight line to a quadratic curve rather than a second-order polynomial as provided from the above model.

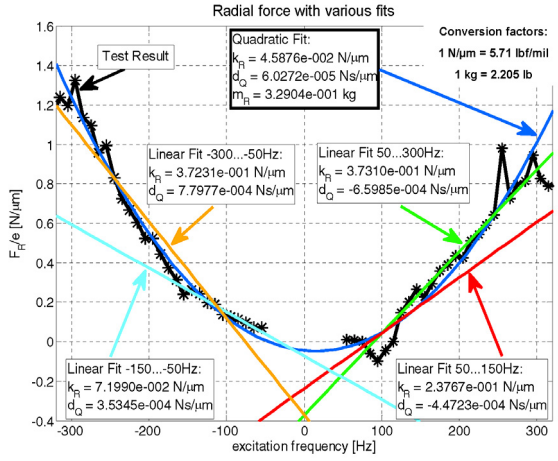

Figure 2. Accidental Stiffness and Damping Numbers of a Quadratic Curve.

SEAL TEST RIG

Test Rig Design

The seal-test rig as shown in a cross-sectional view in Figure 3 was already presented by Wagner and Steff in 1996. It is driven by a variable-speed motor via a gear unit, connected to the test rotor by a quill shaft in order to isolate the dynamics of the motor/gear shafts from the test shaft. Two identical test seals are arranged

symmetrically in the high-pressure barrel type casing to balance the axial thrust. Active magnetic bearings support the test rotor and are additionally able to set the rotor to a static eccentricity and to superimpose a rotor movement on a circular orbit around this point. Frequency, amplitude, and direction of the precession can be set according to the test intent; this movement is independent of the rotor speed. A further task of the magnetic bearings is acting as calibrated transducers for the measurement of the bearing forces, from which the tangential and radial fluid forces can be calculated directly, as shown below.

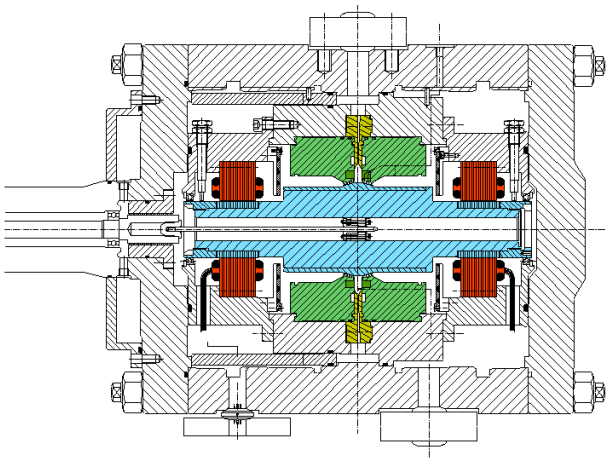

Figure 3. Cross Section of Revamped High-Pressure Test Rig.

The full-scale test rig allows the testing of seals as close as possible to original conditions in every aspect, the geometrical seal parameters match typical high-pressure compressors. The inlet and outlet pressures are controlled separately using electronically controlled valves, so that any pressure ratio can be set independently from the inlet pressure. In order to determine the exact swirl in front of the labyrinths, the static and dynamic pressures are measured directly in front of the labyrinth by means of pitot probes. This means that one of the main influencing variables of fluid forces is determined directly with high accuracy.

With the revamp of the test rig in 2005/2006 the operating range for inlet swirl and excitation frequency was greatly extended, the pressure-control system was improved, and a new active magnetic bearing system was implemented in order to reduce limitations in force capacity, especially for the testing of damper-type seals. A completely new inner bundle reduces the assembly time for test specimen exchange with an improved alignment of the test seals relative to the bearings. The new system as shown in Figure 4 gives the possibility to excite the rotor on a forward and backward precession in an enlarged frequency range, together with a completely new data-acquisition system this results in the possibility to determine the full matrix of transfer functions as described in Schmied, et al. (2002). Some data of this revamped test rig are provided in Table 1.

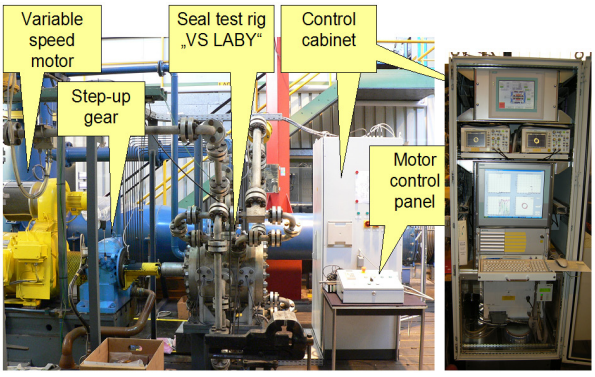

Figure 4. Photography of Revamped Test Rig and its Periphery.

Table 1. Some Operational Parameters of the Test Rig.

Maximum rotational speed	15000. rpm
Maximum inlet circumferential velocity-tested	557.7 ft/s (170. m/s)
Frequency range for shaft excitation (orbit precession)	-400. Hz to +400. Hz
System design pressure	3626. psi (250. bar)
Typical maximum test pressure (inlet)	1015. psi (70. bar)

Development of a Calibrated Test System

The most important process before entering into a regular mode of testing is the systematic calibration of the entire system. Although this is a long-lasting and most challenging task, it is crucial for the quality of all results. The following gives a brief survey on the steps taken:

Component Calibration

The vibration probes, which provide the displacement input for the magnetic bearing control system, were calibrated in situ. High-precision mechanical gauges were placed onto the shaft and records were made of position and voltage, while the shaft was brought to its maximum positive and negative displacement in all axes. The adjusted sensitivity was 228.6 mV/mils (9. mV/μm).

The data-acquisition cards were also calibrated for defined digital inputs. Typical results for the automatic calibration of position and current (force) signals including an averaging of a number of recorded points are given in Figure 5.

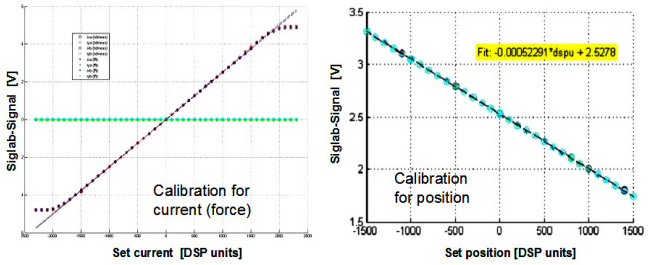

Figure 5. Automatic Calibration of Position and Current (Force) Signals.

The rotor mass is determined after any change made to the rotor with a high-precision scale, providing a mass uncertainty of 0.011 lb (5. gram). Exact knowledge of the rotor mass is important, since the dynamic calibration is based on the rotor inertia.

Required Corrections

Since the system calibration was verified after each step, it was found out iteratively which corrections were required in order to achieve acceptable results.

Correction with *orbit size* (nonlinear effect): A corrective transfer function is determined for orbit radii of 0.236 mils (6. μm) to 0.551 mils (14. μm) in 0.079 mils (2. μm) increments in the entire frequency range from 50. Hz to 400. Hz. This correction predicts a frequency-dependant factor of up to 5 percent. Although the magnetic bearing is designed for a good linearity by choosing a high-bias current, it is nonlinear by nature and even the remaining minor deviations from ideal linearity need to be considered in the calibration procedure.

Thermal effects: Careful calibration-data analysis revealed some impact of the bearing-coil temperature as well as of the entire electronics temperature. For minimization of these effects the control cabinet temperature is held constant by use of a heater and an air conditioner, both being activated by a joint electronic control when needed. Further, the dynamic calibration as used for the seal test data is based on the average of two dynamic-calibration test runs, being recorded immediately before and after each seal-test run.

Correction with *dynamic forces in the magnetic bearing gap* (additional gas force): Gas forces in the system were measured for various pressures and speeds without a labyrinth test seal being installed. Accordingly, these gas forces are caused in the annular air gap of the magnetic bearings and the auxiliary bearings. They were recorded and stored as normalized data for various operating conditions for later subtraction from the total gas force:

$$F_{Laby} = F_{Total,gas} - F_{Bearing,gap} \tag{6}$$

Correction with *dynamic forces in the downstream annulus* (additional gas force in the flow section behind the test seal): Tests with several radial heights between rotor and stator in the section behind the test seal were conducted. Only a minor influence could be detected from the experiments, although the CFD analyses indicated that even small dynamic-pressure amplitudes in this section could have a considerable contribution due to the large cross section, onto which this pressure is acting. No corrections were implemented in the software with this regard, but it was decided to fabricate this radial height as large as possible in order to minimize any additional force contribution.

Correction of *time delays of signals* (data-processing): The need for an analog interface introduces unfortunately a serial data transfer from the magnetic bearing controller to this interface. Time delays between individual data channels cause a phase-shift between data, which needs to be considered adequately in the data processing. Example: A delay of 0.1 ms would result in a phase shift of 14.4 degrees at 400. Hz and would distort the radial/tangential-force ratio accordingly if not considered properly.

Static Calibration

The force-current-characteristic (F,I-characteristic) was determined at the bearing supplier's laboratory for an array of eccentric positions of the journal in the bearing stator (Figure 6). These data form the basis of the static calibration and the determination of magnetic bearing linear coefficients k_i and k_s. In order to obtain a good linear F,I-characteristic in the operating point the magnetic bearings are designed for a high bias current of 7. Ampere.

For the well-known bearing force (rotor mass under gravity only) and a measured bearing-control current it is possible to derive the shaft position relative to the magnetic center from the array of F,I-curves.

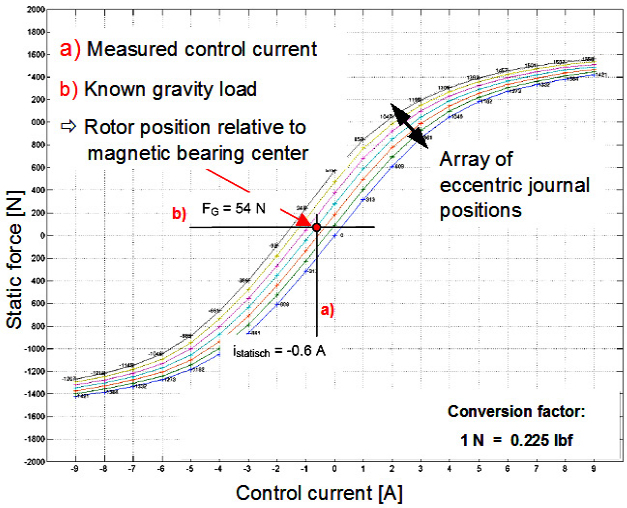

Figure 6. Measured Force/Current-characteristic for Different Eccentricities of the Rotor.

Dynamic Calibration

By means of feeding a proper reference signal into the magnetic bearing control loop the rotor is moved on a circular orbit for various frequencies. For this movement the condition of equilibrium of the magnetic bearing forces with the rotor inertia forces must be fulfilled:

$$F_{AMB} + F_{Inertia} = 0 \tag{7}$$

This allows determination of corrective transfer functions T_i and T_s for the linear bearing coefficients:

$$T_i \; k_i \, \underline{I} + T_s \; k_s \, \underline{x} + T_s \frac{1}{2} m\Omega^2 \underline{x} = 0 \tag{8}$$

with $\underline{I}$ being a current and $\underline{x}$ a displacement indicator, m rotor mass, and Ω precession angular frequency.

Validation of Calibration

Since a number of correction and calibration steps were implemented, the overall system complexity and the data-processing software with a lot of conversions are far from trivial. Therefore the authors looked for means that are suitable for overall validation purposes of the entire calibration rather than relying on proper combination of several localized measures. Ideally, the simplest quantities are used for this validation, like the two following items. An elastic bar with rigid support on one end was mounted and attached to the rotor identically with the quill shaft used for the normal drive as shown in Figure 7. The stiffness of this elastic bar was determined to be k=1.49 lbf/mils (0.26 N/μm) for the nonrotating shaft using the implemented identification software. The direct measurement of this stiffness on a simple external device with rigid support on one end and a precisely known gravity load at exactly the same axial location was k=0.71 lbf/mils (0.125 N/μm).

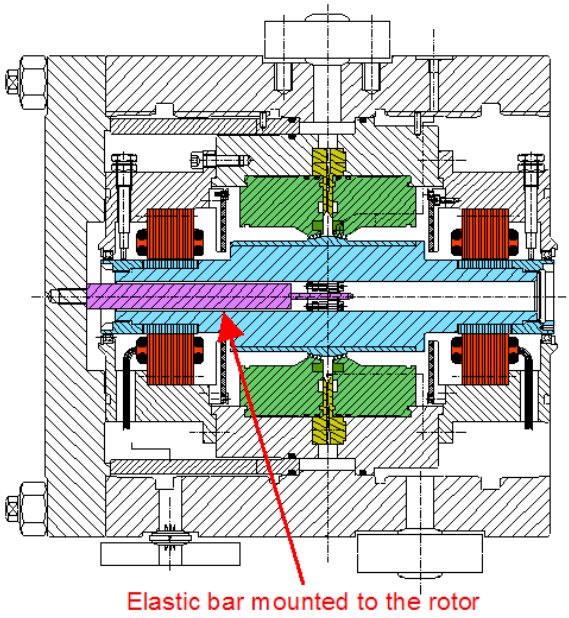

Figure 7. Elastic Bar with Rigid Support for Verification Purpose.

From the difference of these repeated and averaged test values a static accuracy of Δk_{stat}=0.77 lbf/mils (0.135 N/μm) can be derived. Further, different additional masses were attached rigidly onto the rotor according to Figure 8. These masses were also identified by means of the implemented identification software under consideration of all corrections introduced. The attachment of two masses, which were recorded to be 0.661 lb (300. gram) from the scale reading, resulted in a mass of 0.441 lb (200. gram) from the identification algorithm. This deviation of 0.110 lb (50. gram) for the direct inertia m_R of one single seal can be converted into a dynamic stiffness number for one seal by multiplying by squared orbit frequency and this leads to a dynamic accuracy of Δk_{dyn}=1.02 lbf/mils (0.178 N/μm) at 300 Hz. For smaller attached

masses this accuracy was even better, like 0.015 lb (7. gram) deviation for an attached mass of 0.342 lb (155. gram). From these two accuracy figures an average uncertainty of Δk =0.90 lbf/mils (0.157 N/μm) can finally be stated for this identification method.

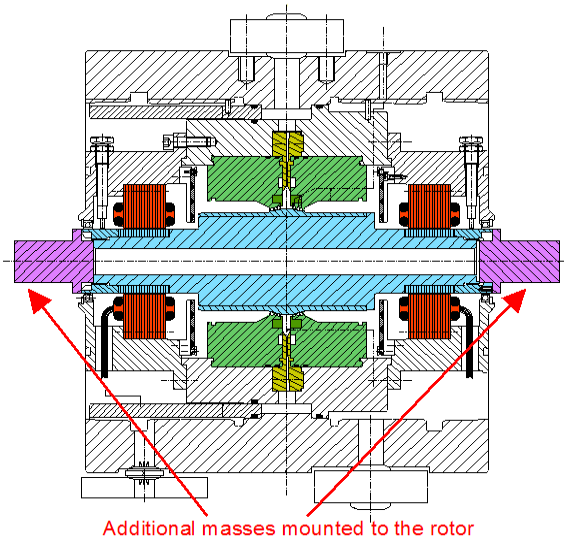

Figure 8. Additional Masses for Verification Purpose.

Another check refers to the identified cross-coupled stiffness and inertia terms, which are of course zero for the two test cases described before. The identification procedure determined these cross-coupled coefficients to be $\Delta k_{Q,stat}$=0.006 lbf/mils (0.001 N/μm) and Δk_{dyn}=0.074 lbf/mils (0.013 N/μm) instead of zero, which is sufficiently close.

Test Procedure

With the developments of the previous section the system is suitable for testing, which comprises *data-acquisition phase* and *data-analysis phase*.

Data-Acquisition Phase

- Static calibration, without gas forces
- First dynamic calibration, without gas forces, but at rotor speed of test
- Adjust specific operating point (inlet pressure, pressure ratio across the seal)
- Perform measurement
- Excite rotor to circular forward precession, orbit radius e=0.394 mils (10. μm), vary frequency in 10. Hz increments from 50. Hz to 400. Hz and hold at each frequency for 2. seconds.
- Repeat previous excitation with backward precession.
- Second dynamic calibration, without gas forces, but at rotor-speed of test
- Save all data for post-processing on the computer system together with all data from thermodynamic data acquisition.

Data-Analysis Phase

- Determine static offset (DC component) of vibration and current (=force) signals. Vibration offset should be zero per control algorithm for zero-DC reference signal. Static forces may exist due to unavoidable minor deviations between seal and magnetic bearing geometrical center.
- Determine applicable force curve from the array as used for static calibration for consideration of static gas forces.
- Determine coefficients k_i and k_s for the static load of this test point, denoted k_i^g and k_s^g.
- Determine total gas forces from the force equilibrium:

$$T_i\ k_i^g\ \underline{I} + T_s\ k_s^g\ \underline{x} + T_s \frac{1}{2} m\Omega^2 \underline{x} + F_{Total,gas} = 0 \qquad (9)$$

by using orbit-amplitude corrections T_i, T_s taken from average of first and second dynamic calibration

- Determine seal forces from:

$$F_{Laby} = F_{Total,gas} - F_{Bearing,gap} \qquad (10)$$

- Decompose the seal force into restoring radial (F_r) and destabilizing tangential (F_t) force components.

Analysis of Overall System Dynamics

While the method as described in the preceding section utilizes statically and dynamically calibrated force and displacement signals from a rotor on a circular orbit, an alternative method based on analysis of the overall system-dynamics of the entire seal-test rig is introduced in this section.

In particular it is possible to generate a detailed model of the rotor and of the complete magnetic bearing system including the electronics. This also allows extraction of seal-gas forces and enables the verification of the impact of the experimentally determined gas forces on the overall system dynamics. Such a comparison would allow an important plausibility check.

For verification purposes a model-based seal-identification algorithm is developed. Basis for this identification method is the measurement of the plant in terms of the control theory and the comparison of the plant with and without the influence of the fluid structure interaction. In the context of this work, the plant consists of the rotor, the bearings, sensors, amplifiers, D/A and A/D converters, zero order hold (ZOH), etc. The control loop is shown in a simplified form in Figure 9.

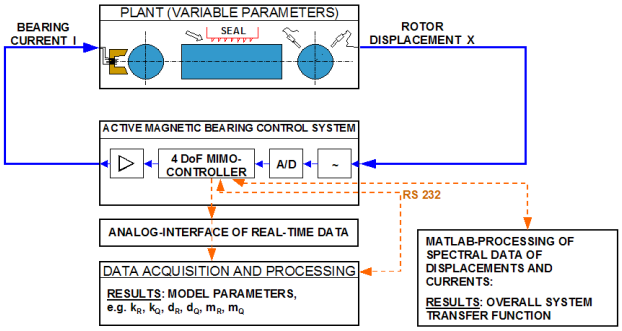

Figure 9. Schematic of the Control Loop, Showing the Test Seal as Part of the "Plant."

The rotor as part of the plant is modeled by finite elements (Timoshenko beam-type elements) with 18 nodes, each with 4 degrees of freedom (DOF), i.e., the axial and torsional DOFs are omitted. The FE-model is shown in Figure 10.

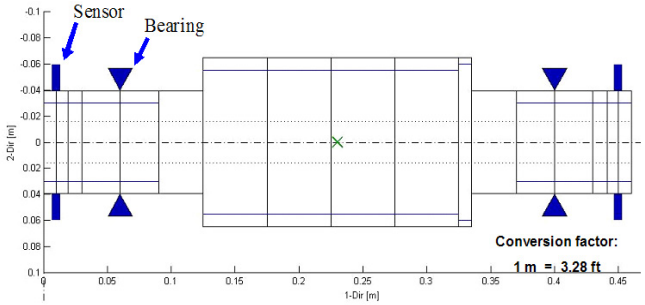

Figure 10. Finite Element Model of the Test Rotor.

As a result of the FE-model, a set of ordinary differential equations is obtained.

$$M\,\ddot{q} + \left(D + \omega G_{gyro}\right)\dot{q} + K\,q = F\,w \tag{11}$$

with rotational speed ω, the mass matrix M, damping matrix D, gyroscopic matrix G_{gyro}, and stiffness matrix K.

q is the displacement vector, F is the input-positioning matrix, and w the force-input vector. Obviously gyroscopic effects are taken into account, enabling the calculation of backward and forward modes at operating speed. Due to the allocation of the input-positioning matrix, the noncollocation of the sensors and the actuators is taken into account.

The transfer functions from the bearings to the sensors (Input: control currents at the bearings, Output: displacements at the sensors) is modeled for all axes, resulting in a 4×4 transfer-function matrix. From the overall plant measurement, the same transfer functions are obtained by "subtraction" of the A/D, D/A, and zero order hold transfer functions. The result of the model is the transfer-function matrix of the rotor in combination with the bearings.

The measured rotor-transfer functions (refer to Figure 11) are compared with the analytical model. As an example only one transfer function (from the x-bearing axis at the left side to the sensors x-axis at the same end) is shown in Figure 11. The first bending mode of the rotor is located at 1400. Hz, i.e., far above the operating-speed range. However, the model is in very good accordance with the measurement. Due to the gyroscopic matrix, a split of backward and forward modes is noticeable.

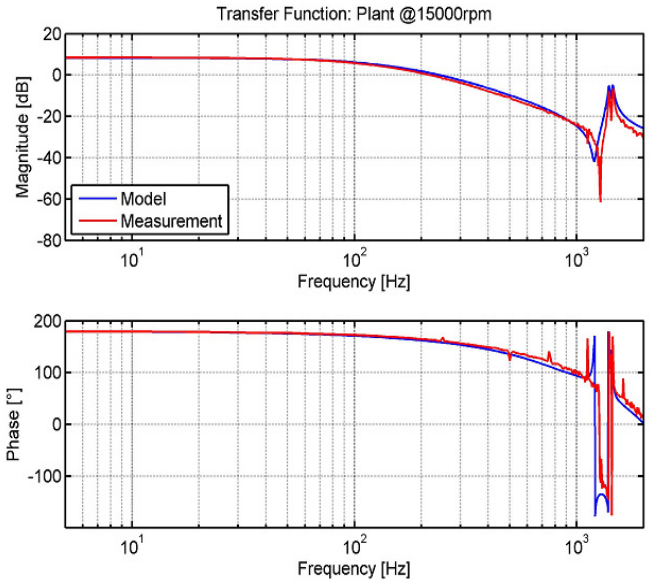

Figure 11. Measured and Calculated Transfer Function of the Plant.

The fluid dynamic force is acting on the rotor node at the center of gravity. The force is assumed to be proportional to the displacements of that node. The force-displacement relationship is modeled by a multiple input multiple output (MIMO) 2×2 transfer-function matrix as defined in the equation below and figuratively shown in Figure 12.

$$\begin{bmatrix} F_1 \\ F_2 \end{bmatrix} = \underbrace{\begin{bmatrix} H_{xx}(j\Omega) & H_{xy}(j\Omega) \\ H_{yx}(j\Omega) & H_{yy}(j\Omega) \end{bmatrix}}_{G_{Laby}} \begin{bmatrix} x_1 \\ x_2 \end{bmatrix} \tag{12}$$

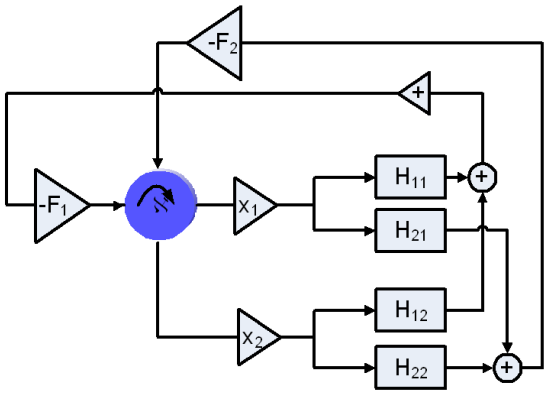

Figure 12. MIMO 2×2 Transfer Function for the Force-Displacement Relationship.

The calibration of the model is performed by replacing the modeled open-loop transfer-function from the bearings to the sensors by the measured transfer functions at test speed without pressure. From the measurement including the influence of the labyrinth seal the gas force is extracted according to Figure 14. The mathematical background for this extraction shall be treated here only in brief. The plant as shown in Figure 13 is defined in the context of this paper as:

$$G_{Plant}(s) = \frac{Y_{Plant}(s)}{U_{Plant}(s)} \tag{13}$$

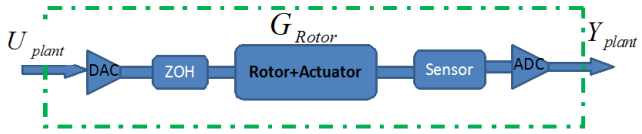

Figure 13. Sketch of the Elements of the "Plant."

The transfer function of rotor and actuator can be determined from the known transfer functions of the sensor system and the ADC and DAC converters by:

$$G_{Rotor+Actuator}(s) = \frac{G_{Sensor}^{-1}\,G_{Plant}}{G_{DA}\,G_{AD}} \tag{14}$$

The inputs of the actuators are the control currents of the four bearing axes; the outputs of the rotor are the displacements at the four sensor locations.

The model is extended by taking into account the seal force acting on the center of the rotor. Since the seal force is acting on the center, the displacement of the center has to be considered as an extra output as indicated in Figure 14, resulting into a 6×6 transfer function matrix.

$$G = \frac{Y}{U} = \begin{bmatrix} G_I^{\,4\times4} & G_a^{\,4\times2} \\ G_b^{\,2\times4} & G_c^{\,2\times2} \end{bmatrix}^{6\times6} \tag{15}$$

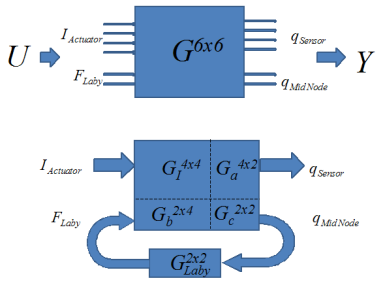

Figure 14. Block Diagrams for Consideration of Seal Forces at Rotor Center.

The result is a transfer function matrix of the order 4×4 for the entire plant including the seal-transfer function:

$$G_{rotor+Actuator} = \frac{q_{Sensor}}{I_{Actuator}} = G_I + G_a G_{Laby} (I - G_c G_{Laby})^{-1} G_b \qquad (16)$$

The calibration of the model is performed at test speed without the labyrinth force, i.e., G_{Laby}=0. The rotor is excited within each bearing plane (translation and tilting) and the transfer functions of the plant are calculated from the recorded signals. The transfer functions are reduced by those from the known transfer functions of the electronic devices (sensor, D/A, and A/D converter) and the remaining transfer functions of the rotor and actuator are used for the seal-force identification in the following.

In a first step the measured rotor and actuator transfer functions are used instead of G_I in Equation (16). In a next step the plant is measured at the same speed but with the influence of the labyrinth seal forces at test pressure. The 2×2 transfer-function matrix of the labyrinth forces can be obtained after some easy conversions of Equation (16):

$$G_{Laby}^{2\times 2} = (I + G_x G_c)^{-1} G_x \qquad (17)$$

with:

$$G_x = (G_a^T G_a)^{-1} G_a^T (G_{rotor} - G_I) G_b^T (G_b G_b^T)^{-1} \qquad (18)$$

A typical result for the four elements of the transfer function matrix $G_{Laby}(s)$ of the labyrinth-seal forces determined by this method is shown in Figure 15.

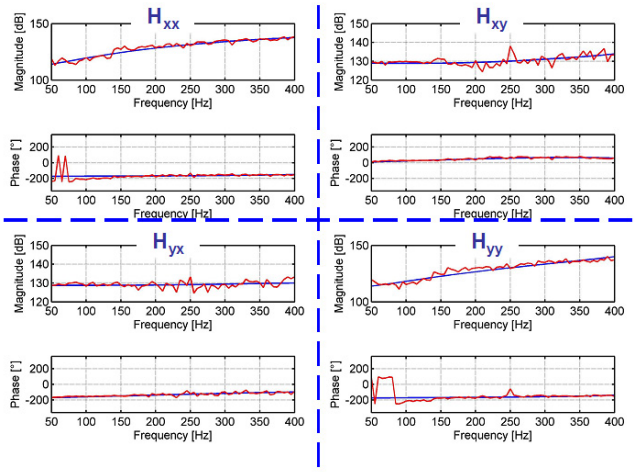

Figure 15. Typical Results for Transfer-Function Matrix of the Labyrinth Seal Forces.

Based on the identified transfer functions, it is possible to calculate radial and tangential forces if the rotor is excited on a circular motion about the center of the seal. Usually the seal transfer functions are considered skew symmetric according to Equation (1). For this special case, the radial and tangential forces are the same in relation to the position, because of the circular motion and the axis symmetry of the seal.

NUMERICAL ANALYSIS

General Aspects on the Use of CFD

In the 1980s analytical approaches based on bulk-flow models were developed using one, two, or three control volumes. On the one hand these models can be solved very fast on a simple computer; on the other hand they require empirical corrections to match theory and experimental data.

During recent years the commercial tools for computational fluid dynamics were further improved significantly. The combination of sophisticated solver technologies and enhanced capabilities of modern workstation computers allows the usage of detailed models, which are required to predict dynamic seal forces. CFD tools nowadays allow the simulation of the flow field with different approaches. The spectrum available covers rotating domain simulations with transient and steady-state simulation up to moving mesh simulation in a stationary domain. Interfaces are required to couple rotating and stationary parts of the calculation regime. For the authors' studies a fluid flow analysis and design optimization software is used. This software is widely used within the turbomachinery community. Multigrid solvers in combination with parallel processing allow the usage of detailed CFD-meshes adequate for labyrinth-flow simulation. For the simulation of the test rig no strong influences of rotor/stator interaction effects were expected. Therefore no transient simulations were necessary. All simulations were performed in a rotating-relative system.

CFD for Prediction of Dynamic Seal Coefficients

To predict dynamic seal properties the selected approach follows many other researchers; a number of interesting publications are cited in the bibliography. The authors consider an idealized model of a rotor with a spinning frequency ω rotating around the center of the stator on a circular orbit with whirling frequency Ω and orbit radius e. These model assumptions are shown in Figure 16 /left. This transient problem can be transferred to a stationary one using a rotating relative system as shown in Figure 16 /right. The following boundary conditions are used:

- The gap between rotor and stator is regarded as a rotating-relative system.
- The relative system rotates with orbit frequency Ω.
- The circumferential velocity of the walls are defined relative to the orbit, i.e., the shaft surface rotates with a frequency Ω_{rel} =(ω−Ω), while the stator surface rotates at Ω_{wall} =(−Ω).
- The upstream and downstream parts of the test rig are defined in a fixed absolute system.
- Using a multiple frame of reference (MFR) software, the flow in all individual parts can be handled as stationary. The coupling between the reference systems can be handled using the so-called "frozen rotor" interface, averaging flow and variables in circumferential velocity.

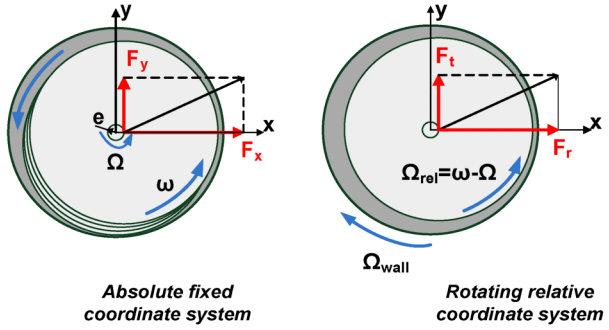

Figure 16. CFD Coordinate Systems.

The forces acting on the rotor are calculated via integration of pressure distribution along the surface. Forces generated by shear stresses are very small and can therefore be neglected.

$$F_x = -\iint p \, dA_x = \iint p \cos\varphi \, dA \qquad (19)$$

$$F_y = -\iint p \, dA_y = \iint p \sin\varphi \, dA \qquad (20)$$

For a circular motion around the center of the stator, seal forces can be modeled according to Equation (5). To determine the dynamic-seal properties the rotor is shifted in the plane (x,y) vertical to the axis of rotation (z), i.e., with an orbit eccentricity of $\underline{E} = [e_x, e_y]$. For the time t=0, the orbit eccentricity is reduced to $\underline{E}(t=0) = [e_x, 0]$.

Table of Contents

For CFD simulation in the relative system the rotor is moved in the x-direction. At time t=0 the x-direction is identical to the radial force direction and the tangential forces can be assigned to the forces in the y-direction. From the equilibrium of forces the following two equations can be derived:
Radial forces (x-direction):

$$\frac{F_x}{e_x} = \frac{F_r}{e_x} = -k_R - d_Q\,\Omega + m_R\,\Omega^2 \qquad (21)$$

Tangential forces (y-direction):

$$\frac{F_y}{e_x} = \frac{F_t}{e_x} = k_Q - d_R\,\Omega - m_Q\,\Omega^2 \qquad (22)$$

Based on these formulae, the quotients of forces acting versus rotor eccentricity can be approximated via second-order polynomial functions of orbit frequency Ω. Therefore CFD simulation results must be available for at least three different orbit frequencies to allow identification of the seal stiffness, damping, and mass coefficients, for example via least square fit. It will be shown in a later section that more than three frequencies have been predicted in order to capture with certainty the right curvature.

Mesh Generation and Boundary Conditions

The simulation of the flow-through labyrinth seals requires high-quality CFD meshes. In the axial and radial directions extremely high gradients of velocity and pressure occur that must be resolved sufficiently. The need to mesh a complete 360 degree model with an excessive number of nodes with increasing numbers of tips also enforces good grids to minimize computational time to achieve convergence.

An automatic mesh-adaptation implemented in the fluid flow analysis software was a good first step to optimize the mesh quality. For these studies only hexahedral meshes were considered. In some published CFD studies tetraeder meshes are used, which can be generated much more easily, but will not be able to provide the required accuracy of prediction. Starting with a coarse grid the mesh refinement is done automatically, driven by calculated gradients. Because the numerical quality (aspect ratio, deformation) decreases significantly along this automatic mesh adaptation, this approach cannot be used for meshes required here. Nevertheless this method gives a good impression of the topology of an optimized mesh. An example for this mesh refinement is given in Figure 17.

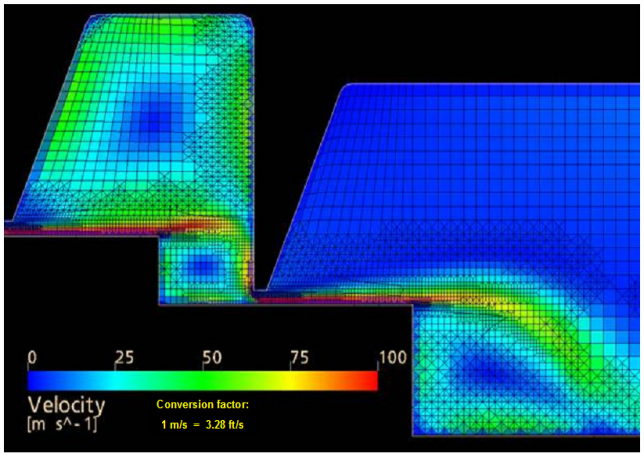

Figure 17. Example for Automatic Mesh Refinement with Superimposed Velocity Distribution.

To ensure that the CFD-simulation results are free of mesh influences in pre-studies the mesh generation was studied systematically, applying the method of "best practice guidelines" (BPG). For most of these studies two-dimensional meshes were used, because the gradients in the circumferential direction are relatively small compared to the axial and radial directions. In Figure 18 the steps of grid-refinement for this study are shown as an example.

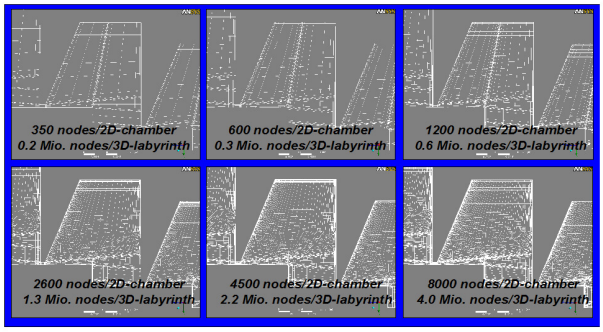

Figure 18. Steps of Systematic Mesh Refinement.

Following the BPG approach, the mesh density is increased until the chosen target ceases to change significantly. For this CFD simulation, the forces acting on the rotor and the mass flow are the first choice, being the target function. As an example, Figure 19 shows the trend of the calculated mass flow versus the number of nodes.

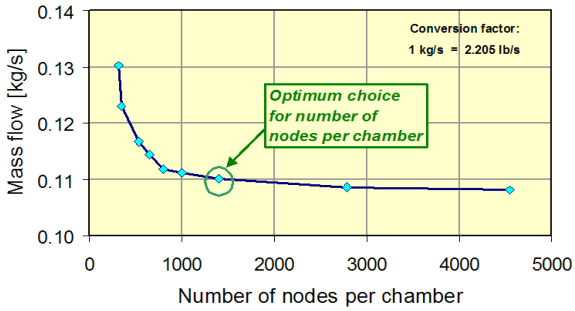

Figure 19. Predicted Mass Flows as Target Function Versus Mesh Density.

This makes it obvious that BPG is a good tool to derive a distinct optimum choice for the mesh. In combination with an optimal distribution of nodes in the boundary layer and a very carefully designed expansion ratio as well, which cannot be explained here in detail, the mesh size can be reduced significantly, e.g., 150,000 nodes for one labyrinth tip/chamber 360 degree model provided good results.

CFD Simulation of the Test Rig

The focus of the CFD study described here is on the short labyrinth seal as a test object in the test rig. But from the start it became obvious that the simulated complete flow path in combination with an adequate choice of boundary conditions has a significant impact on the results. Therefore several geometry configurations with different boundary conditions as shown in Figure 20 were examined by CFD simulation.

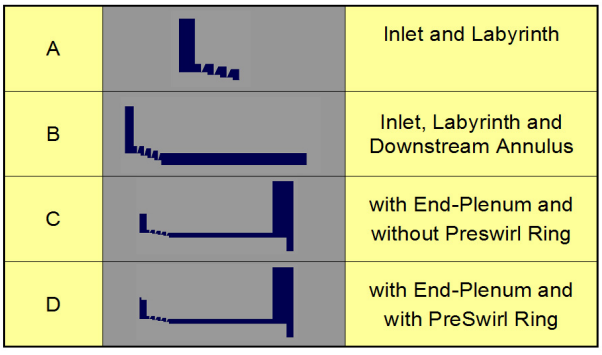

Figure 20. Different Models Used for the Test Rig Simulation.

A simulation concentrated only on the seal tips (option A) in conjunction with simplified boundary conditions is practiced and published by some researchers. However, this approach will not be able to incorporate nonuniform pressure distributions in front of and behind the seal in the circumferential direction and thus cannot predict the reality adequately. A very sensitive part for the CFD simulation is the adequate formulation of boundary conditions. This is especially of importance in the combination of high-pressure and high circumferential velocities at the upstream part. For the downstream part the assumption of constant pressure will generate unrealistic swirl degradation. Using the realistic flow volume at inlet including the swirl apparatus and outlet region of the labyrinth seal (option D) it was possible to improve the simulation efficiently regarding quality of the results and convergence behavior. Based on this experience a detailed mesh of the test rig including upstream and downstream parts can be set up as shown in Figure 21 and Figure 22.

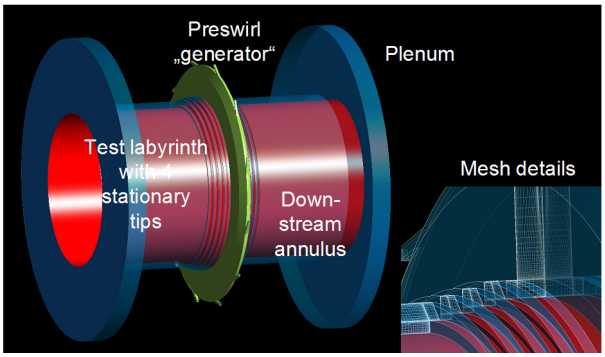

Figure 21. 3D View of the Simulation Model of the Test Rig.

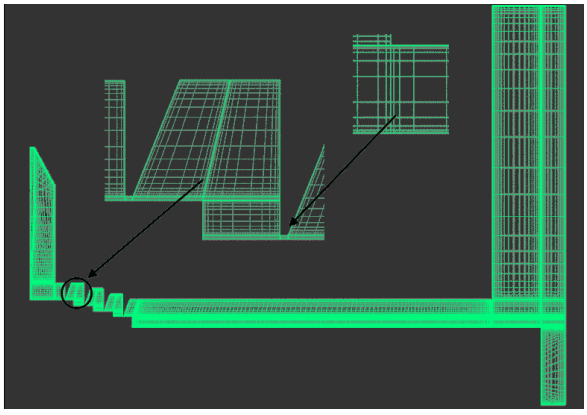

Figure 22. Mesh Details as Used for the Simulation of the Test Rig.

Because the CFD results shall be compared in detail with available test data, the boundary conditions must be modeled precisely. The easier part is the downstream area where a constant static pressure can be applied according to the reality in the test rig. A formulation of the boundary conditions in the upstream part is more demanding because of the very high circumferential velocities that can generate secondary flow in combination with very low meridional velocity typical for seal flow conditions. Using all speed components of the flow as boundary conditions, an additional iteration loop around CFD is required to adjust the static pressure additionally. In the end it was decided to integrate the complete swirl-generating device into the CFD model. This gives the best confidence that flow phenomena resulting from the upstream area are simulated close to the reality and faults resulting from simplified boundary conditions are avoided.

CFD Results for the Test Rig

Only some aspects can be highlighted here for the calculations for the geometry as provided in the section “COMPARISON TEST RESULTS/NUMERICAL ANALYSIS.” The matching of very small meridional velocity, high swirl, and wall boundary conditions generates a distinct flow profile with vortices in the labyrinth chambers as shown in Figure 23. This supports the statement that the results are sensitive to the upstream flow conditions.

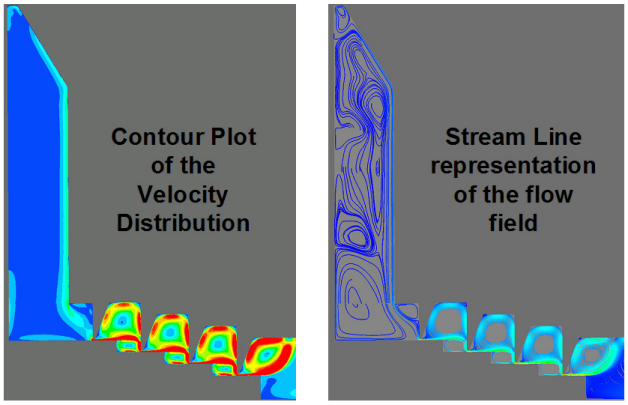

Figure 23. CFD Results in Terms of Test Rig Velocities and Stream Lines.

Another important result from the CFD studies is the finding that the annular downstream area following the last labyrinth-seal tip has a significant influence on the flow field. It is mainly that part of the mesh that leads to a longer period of simulation to achieve convergence. Counter-rotating vortices as shown in Figure 24 can develop in the gap and in the large cavity. The radial and tangential forces generated downstream of the seal cannot be neglected.

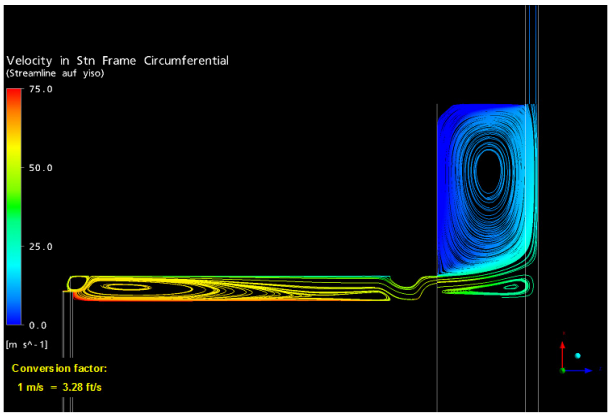

Figure 24. Predicted Vortices in the Downstream Annulus.

These results from comprehensive test rig simulations indicate the need to consider the real geometry upstream as well as downstream of a labyrinth seal within a real compressor. Numerical results of these CFD simulations in terms of radial and tangential forces are provided in the following section.

COMPARISON TEST RESULTS/ NUMERICAL ANALYSES

Seal Geometry Data and Operating Points

The scope of testing of impeller-eye seals covers, of course, variations in the seal geometry as well as in the operating parameters speed, inlet pressure, and pressure ratio. However, for the sake of an in-depth comparison of the results as derived from application of different methods, the results will be compared for a single test point in Figure 28 through Figure 33 for the data as provided in Table 2. A drawing of the labyrinth details as well as the arrangement of the pair of test seals in the test rig is given in Figure 25.

Table 2. Geometrical and Operational Data.

Number of tips [-]	4	Rotational speed	15000. rpm
Tip pitch	0.157 in (4.0 mm)	Inlet swirl	321.5 ft/s (98. m/s)
Tip height	0.157 in (4.0 mm)	Static inlet pressure	290.1 psi (20. bar)
Radial gap width	0.0039 in (0.10 mm)	Inlet temperature	49.7 °F (283 K)
Axial tip width	0.0079 in (0.20 mm)	Static outlet pressure	232.1psi (16. bar)
Radial step height	0.0394 in (1.0 mm)	Gas: nitrogen	61.7 lb/kmol (28. kg/kmol)
Diameter under 1st tip	5.135 in (130.44 mm)	Measured leakage	0.154 lb/s (0.07 kg/s)

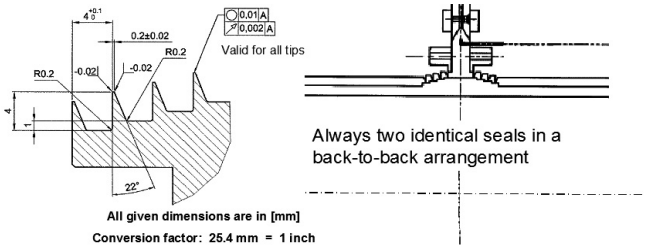

Figure 25. Detail of Labyrinth Geometry and Arrangement of Pair of Test Seals.

Comparison of Dynamic Pressures

The final seal data that are used in the rotor-stability analysis are the dynamic coefficients and thus their direct comparison is of primary interest. However, various effects may have affected these numerical and experimental results and may have led to some deviations. Therefore it is not only of interest, but also adding value to this comparison, if further quantities could be utilized. In the numerical analysis there are, of course, a large number of intermediate results accessible. However, it is quite challenging to upgrade an existing high-pressure test rig with further probes.

As meaningful and feasible intermediate quantities the dynamic pressures within the labyrinth cavities were identified. For this purpose one test seal was machined in such a way that circumferentially spaced and axially inserted dynamic pressure probes were linked to each cavity of a typical impeller-eye labyrinth seal as shown for one cavity in Figure 26. For such a measurement careful consideration of the distance between probe head and cavity, signal amplitude, and frequency range, and in particular a high-quality manual implementation are important in order to avoid false results.

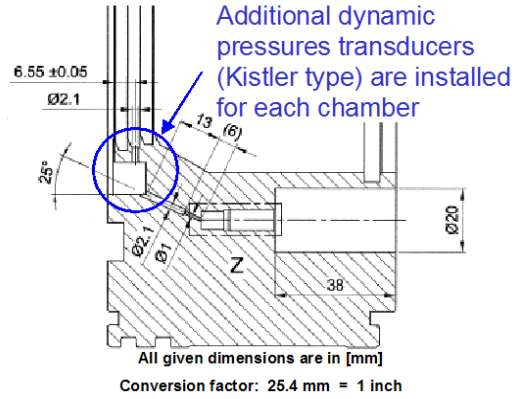

Figure 26. Dynamic Pressure-Probe Arrangement in Impeller-Eye Labyrinth Seal.

Comparison of Dynamic Pressure Amplitudes

In a first step, the dynamic pressure amplitudes were analyzed irrespective of their phase angle relative to the orbiting rotor. A typical spectrum of this dynamic pressure probe in cavity 1 for a rotor precession of −175. Hz (backward precession) is given in Figure 27. In addition to the peak of 0.580 psi (40. mbar) at precession frequency further pick-up peaks at multiples of the 50. Hz grid frequency are visible as well as multiples of running speed (250. Hz). Since this is likely to be a sensitive kind of measurement and in order to get reliable data, this test point was measured independently six times on different days. All the scattered points and their curve fits are shown in Figure 28.

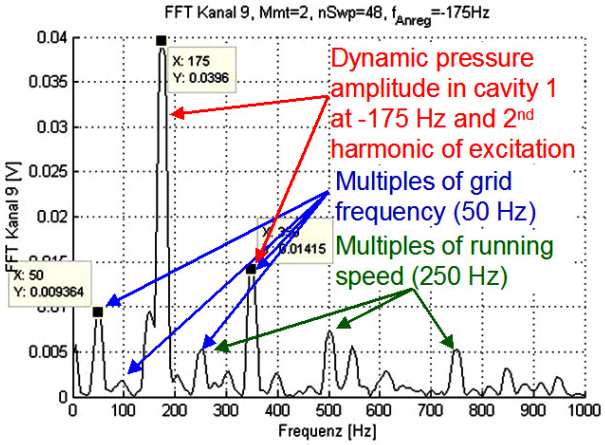

Figure 27. Spectrum of Measured Dynamic Pressure in Seal Cavity.

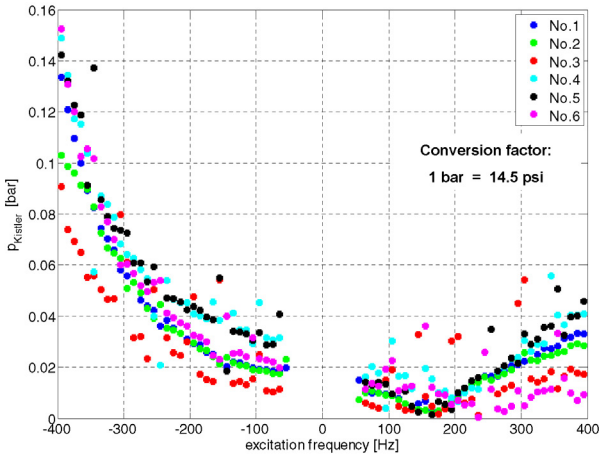

Figure 28. Repeated Measurements of Dynamic Pressure in Seal Cavity 1.

For a meaningful comparison with the CFD-calculated dynamic pressures these curve fits of the scattered data are averaged. Figure 29 provides for all three cavities the mean value from the measurement as well as the corresponding standard deviation. The red triangles indicate two CFD-calculation dynamic pressures for five frequencies in total. These two different values are obtained from reading a line of infinitesimal width (leading to lower values) and from a line of 0.028 in (0.7 mm) width (being identical with the effective width of the hole for the measurement, leading to the larger values), which were used during the course of post-processing. With plotting these two values per frequency it is intended to demonstrate exemplary uncertainties being involved not only in experiments, but also in post-processing and analyzing numerical results. The agreement of test and prediction is quite good, although it seems that the CFD-calculation has a trend in particular for cavity 1 to stay below the mean value of the measurement.

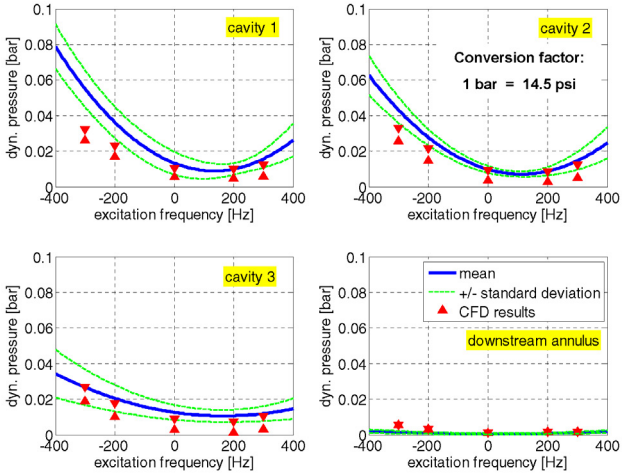

Figure 29. Comparison of Averaged Measurements and CFD-Predicted Dynamic Cavity Pressure.

Interesting to note is the fact that both measurement and prediction indicate a quadratic (or even higher order) relationship with respect to frequency. This is evaluated to be a substantial new insight, since these short impeller-eye seals have previously been either neglected or considered to behave like a spring/damper system. Since the curvature as given in Figure 29 can be fitted very well with a second-order fit, this can be interpreted as an inertia effect of the gas confined within the eye seal.

The achievement of this result is attributed primarily to the test rig's capability of taking measurements over a relatively wide frequency range and by doubling this range through tests with forward and also with backward precession.

Consideration of Dynamic Pressure Phase Angles

Although the comparison of the dynamic-pressure amplitudes provides important insights, the phase angle needs to be incorporated into the analysis in order to evaluate the dynamic pressure profile in terms of tangential and radial components. The realization of such an analysis requires a lot of care in consideration of the different trigger points for the forward or the backward precession as well as the circumferential location of the individual dynamic pressure probe. With an appropriate processing of the acquired data these effects were considered and finally allowed also a judgment on the tangential and radial components of these dynamic pressures.

$$\begin{pmatrix} F_x \\ F_y \end{pmatrix} = -\int_0^L \int_0^{2\pi} p(\varphi)\, r \begin{pmatrix} \cos\varphi \\ \sin\varphi \end{pmatrix} d\varphi\, dz \;=\; -\pi\, \hat{p}\, r\, L \begin{pmatrix} \cos\beta \\ \sin\beta \end{pmatrix} \qquad (23)$$

The composition of the radial and tangential force from the direct and cross-coupled coefficients is shown in the equation below, whereby relating this force to the orbit amplitude e converts these forces into dynamic stiffnesses in N/µm.

$$-\frac{F_r}{e} = k_R + \Omega\, d_Q - \Omega^2 m_R \qquad -\frac{F_t}{e} = -k_Q + \Omega\, d_R + \Omega^2 m_Q \qquad (24)$$

In Figure 30 these radial and tangential components of the pressure were multiplied with the respective seal area in order to arrive at the forces, which are then related to the orbit amplitude. In qualitative agreement with Figure 29 a clear quadratic shape can be seen for the radial dynamic stiffness (upper diagram), pointing to a gas-inertia effect in the restoring direction. The tangential dynamic stiffness (lower diagram) exhibits an almost straight line, which can be represented by a cross-coupled stiffness and direct damping; the cross-coupled inertia effect is negligible. A measure for the uncertainties involved is the standard deviation, which is plotted in addition to the mean value of several measurements.

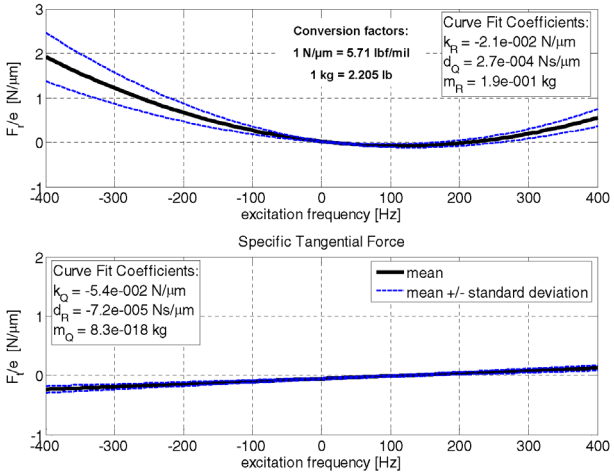

Figure 30. Radial and Tangential Forces as Derived from Dynamic Pressure Measurement Within the Seal Cavities.

Radial and Tangential Forces
Derived from the Magnetic Bearing System

Two different methods were employed in order to determine the seal gas forces via the magnetic bearing system: While the first method utilizes statically and dynamically calibrated force and displacement signals from a rotor on a circular orbit, the second method is based on analysis of the overall system dynamics of the entire seal-test rig when excited in one direction only. For both methods, the forces that were generated in the annulus of the magnetic bearing, have to be subtracted from the measurement as described earlier in order to separate the forces originating from the test seal.

Results from the first method (circular orbit) are shown in Figure 31. Obviously the radial force results (upper diagram) are in quite good agreement with the result from the dynamic pressure as provided in Figure 30. Again, the quadratic shape of the curve confirms the existence of the direct inertia term of the gas.The tangential force (lower diagram) is here also an almost straight line; however, slope and magnitude differ from the result obtained from the dynamic pressure.

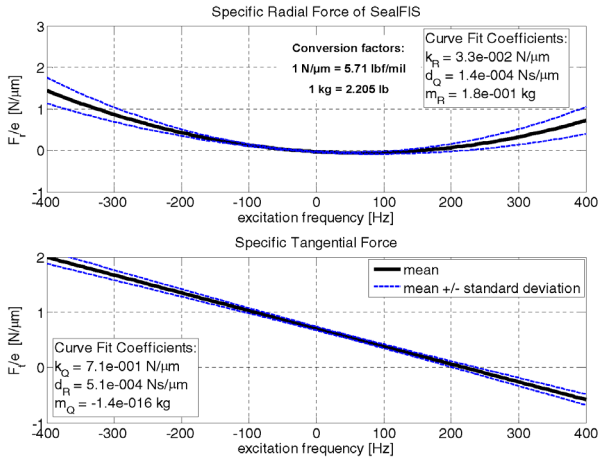

Figure 31. Radial and Tangential Forces as Derived from the Magnetic Bearings for a Circular Orbit.

The results obtained from the second method (based on analysis of the overall system dynamics) are given in Figure 32. For the radial force (upper diagram) the quadratic shape of the curve is confirmed again, although the magnitude and in particular the curvature is smaller compared with the result from the circular orbit and from the dynamic-pressure measurement.

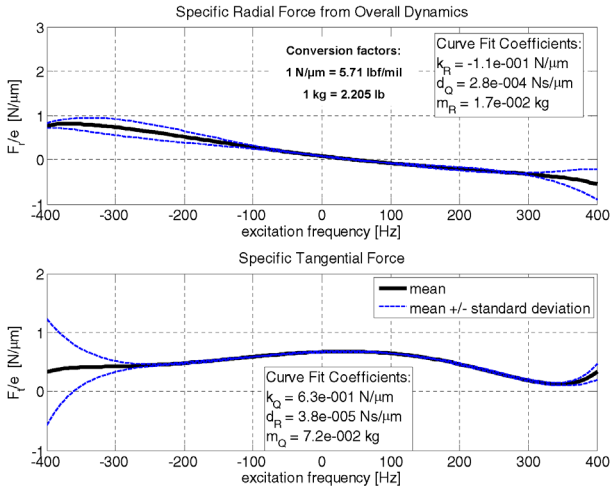

Figure 32. Radial and Tangential Forces as Derived from the Overall System Dynamics.

The tangential force (lower diagram) is in deviation from all other methods here a curve with a slight S-shape, what does not suit any of the popular spring/damper/inertia models. However, when only the frequency range from −300 Hz to +100 Hz is evaluated, then the slope of the curve (i.e., direct damping) is very close to the results as derived from the dynamic pressure measurement. The magnitude of the tangential dynamic stiffness curve (=specific force) at frequency zero has the meaning of representing the cross coupled stiffness k_Q. This important quantity, driving a rotor system unstable, is very close for both methods based on the magnetic bearing forces.

Radial and Tangential Forces Derived from the Numerical CFD Analysis

In a previous section, the CFD-predicted dynamic pressures in the individual cavities have been compared with the measured dynamic pressures. It was found that the CFD-calculated dynamic pressures were somewhat lower than the measured dynamic pressures. The spread of the numerical values for the dynamic pressure, caused by different methods of performing this reading, is eliminated when looking to the forces, because these forces are determined by numerical integration of the entire pressure profile. These predicted forces are shown in Figure 33. It shall be noted that the predicted inlet swirl of 331.4 ft/s (101 m/s) at the location of the pitot tube, which is a most important quantity affecting the seal forces, agrees very well with the measured inlet swirl of 321.5 ft/s (98 m/s).

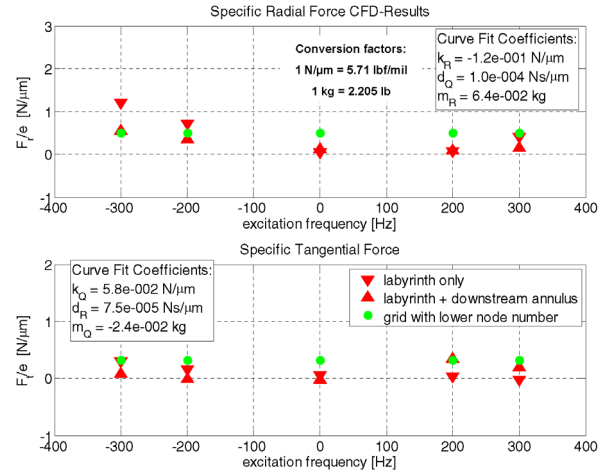

Figure 33. Radial and Tangential Forces as Derived from CFD Analysis.

The different symbols in these graphs are related to an integration of the pressure profile:

- Only within the seal area and
- For the entire area including the downstream annulus.

While this downstream annulus does not play a role in the comparison with the forces as determined from the measured dynamic pressures in the seal cavities, both experimental methods using the magnetic bearing forces unavoidably include this downstream area in the seal result. The green symbols refer to the results as obtained from an analysis with a grid with reduced node number, indicating the grid effect on the curvature of this graph.

Again a quadratic curve shape is found for the radial force (upper diagram), with a magnitude between the result from the overall dynamics and from the dynamic pressure measurement. The latter comparison is consistent with the result discussed earlier, that CFD seems to under-predict the measurement slightly.

For the tangential force (lower diagram) CFD predicts the smallest value of all four methods. Although the presented diagram might suggest that the tangential force is virtually zero, this does not hold true in general. As analyzed for other conditions the tangential force as predicted per CFD may become more significant than in the test case provided here. This is also confirmed clearly by field experience.

Regarding the confidence in the accuracy of the different experimental methods, it should be considered that the forces generated in the short impeller-eye seals are small quantities and that the two methods based on the magnetic bearing force suffer dynamic effects generated in the annular air gap of these bearings and in the downstream annulus behind the test seal. These effects have been corrected as good as possible, but they are adding uncertainty. From this and from comparison of all of the presented curves the results obtained from the dynamic pressure measurement provide the highest level of confidence for these short seals.

However, for typical balance drum seals, the high tip count leads to a large seal length and much higher forces. Here the aforementioned dynamic effects generated in the annular air gap of the magnetic bearings and in the downstream annulus behind the test seal play a less important role. Instrumentation of such long seals with dynamic pressure transducers in each cavity and analysis of all these data indicate a preference for the two methods based on the magnetic bearing force for this kind of seals. The integrating nature of these methods makes them also to the first choice for damper seal testing.

FURTHER RESULTS AND OUTLOOK

The first task of the CFD study is the comparison of numerical simulations with experimental data including the specification of the requirements for proper modeling and setting of boundary conditions. Consequently, the second task is focused on the application in centrifugal compressors, i.e., the consideration of the applicable boundaries.

One of the results mentioned above is the importance of the upstream and downstream areas of the analyzed labyrinth. For an impeller-eye seal the upstream area of importance is formed by the shroud cavity. With the numerical results of the test rig as shown in Figure 23 it is quite straightforward to consider the shroud cavity and a part of the impeller outlet/diffuser inlet section in the model as shown in Figure 34. This is certainly the most accurate way to predict the correct pressure and inlet swirl at the seal entry.

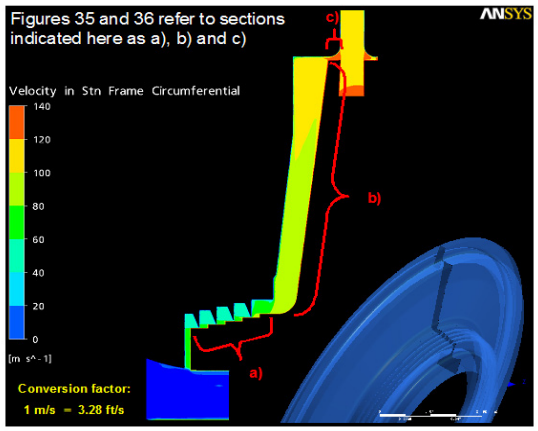

Figure 34. CFD Results for the Flow Path from Impeller Outlet to Impeller-Eye Seal.

Having the flow along the cavity incorporated in the model, it is only one further step to predict the pressure profiles acting on the impeller shroud by basically the same methodology as applied for the seal itself. Such an analysis would then allow predicting both the forces generated in the shroud cavity as well as within the impeller-eye seal. In Figure 35 the radial force and in Figure 36 the tangential force is shown. The overall forces acting on the impeller are presented together with the shares of the individual sections of flow:

a) From the area of the labyrinth seal (input data different from Table 2)

b) From the shroud area in front of the first labyrinth tip up to the outer diameter of the impeller

c) From the axial length of the shroud thickness at the outer diameter of the impeller

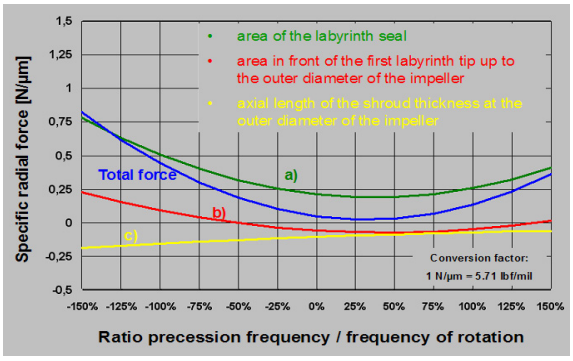

Figure 35. CFD Results for the Total Radial Force on the Shroud and its Buildup.

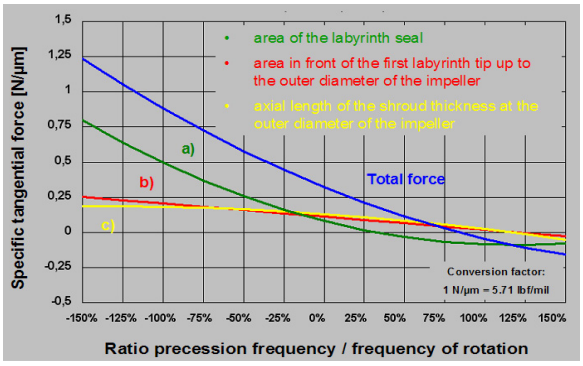

Figure 36. CFD Results for the Total Tangential Force on the Shroud and its Buildup.

From these results it is evident that the labyrinth seal (a), illustrated by the green curve, has the largest effect on the total force, given by the blue curve. The other areas (b) and (c) have about the same magnitude in their contribution and are smaller than the labyrinth force. It is interesting to note, that the relatively short area (c) provides a force as large as area (b)! As mentioned earlier, for this example the tangential (destabilizing) force of the labyrinth is by no means negligible, as it could be derived from the specific operating point of the test rig as shown above in great detail.

The geometry of the impeller as shown in Figure 34 to Figure 36 is taken from another in-house test rig, which is dedicated to research on fluid/structure interaction. This rig is equipped with dynamic pressure transducers, which are embedded in the shroud surface and a multichannel telemetric system. The primary target of this project is analysis of the interaction of Tyler/Sofrin-modes with acoustics in the shroud cavity and structural vibrations of the impeller as outlined in König, et al. (2009). This might offer opportunities in a future phase of testing to correlate these measurements with the CFD predictions in a similar way, as has been shown in this paper for the impeller-eye seal.

CONCLUSION

The core element of this project is a revamped test rig, which enables measurements to be taken up to a frequency of more than 400. Hz; the rotor can be moved on a circular orbit in forward as well as in backward direction. This feature allows determination of the complete set of general seal-transfer functions.

Very high efforts were related to the static and dynamic calibration of the system and its validation. The important determination of the residual uncertainty is often missing in other experimental work. This is of particular importance for the investigation of the short impeller-eye seals, which are very hard to measure, since they cause much smaller forces than the long balance-drum seals. To the authors' knowledge this has not been done successfully before.

A key issue of this paper is the comparison of the results as obtained from different methods. It is unique to determine the stiffness, damping, and inertia coefficients of impeller-eye seals by two different methods of force measurement using the magnetic bearings, by measurement of the dynamic pressures in all seal cavities, and also by computational fluid dynamics and to compare all these results with each other.

One important finding is the evidence of the existence of gas inertia forces in these labyrinth seals. They were verified in particular in the radial force with all four methods.

Computational fluid dynamics is a powerful tool to complement the experimental work. The first step was the detailed CFD analysis using best practice style CFD meshes to calculate the dynamic properties of the seals tested. With the available test data it was possible to fine-tune and calibrate the CFD analysis. Based on this combined knowledge additional numerical results can be generated for geometry variations that are not tested. This approach will enhance the database to cover in the end the complete range of geometries of relevance for turbocompressors from small to large sizes and from low- to high-pressure applications.

Based on numerical analysis, additional effects of importance within a real compressor will be addressed. Here the labyrinth-seal inlet-conditions of impeller-eye seals and the effects of the forces generated in the shroud cavity shall be mentioned as examples of these effects. As an example, one result of these effects showed that the forces of the impeller-eye seal are larger than the forces acting onto the impeller shroud. However, further work needs to be done in this field.

All analytical and experimental data are merged into a simplified tool for the designers' day-to-day work. With this tool, parameter studies and rotordynamic optimizations can be handled easily and effectively.

NOMENCLATURE

A	= Projected area, surface on which pressure distribution acts
d_R,d_Q	= Direct, cross-coupled damping of test seal
D	= Damping matrix
$D(s)$,$E(s)$	= General transfer functions in Laplace domain
e	= Orbit radius of rotor circular precession
e_x,e_y	= Orbit eccentricity in x-, y-direction
$\underline{E}$	= Vector of orbit eccentricities = (e_x, e_y)
F	= Input positioning matrix
F_1,F_2	= Fluid dynamic force in 1-, 2-direction
F_{AMB}	= Magnetic bearing force
$F_{Bearing,gap}$	= Gas forces caused in annular air gaps of magnetic bearings and auxiliary bearings
$F_{Inertia}$	= Rotor inertia force
F_{Laby}	= Gas force caused by labyrinth
$F_{Total,gas}$	= Total gas force
F_r,F_t	= Seal forces in radial and tangential direction
F_x,F_y	= Seal forces in x-, y-direction
G_{gyro}	= Gyroscopic matrix
G	= Transfer function of control currents and labyrinth force to displacements at sensor and mid node
G_{AD},G_{DA}	= Transfer function of ADC, DAC converter
$G_I^{4\times4}$,$G_a^{4\times2}$,$G_b^{2\times2}$,$G_c^{2\times2}$	= Submatrices of transfer function G
G_{Laby}	= MIMO 2×2 transfer function
G_{Plant}	= Transfer function of plant
$G_{Rotor+Actuator}$	= Transfer function of rotor and actuator
G_{Sensor}	= Transfer function of sensors
H_{xx},H_{xy},H_{yx},H_{yy}	= Transfer functions bearing control current to displacements at sensors
$\underline{I}$	= Measured current
$I_{Actuator}$	= Vector of control currents of four bearing axes
j	= Imaginary unit $\sqrt{-1}$
k_i,k_s	= Linear coefficients of magnetic bearing
k_R,k_Q	= Direct, cross-coupled stiffness of test seal
Δk_{stat},Δk_{dyn}	= Static, dynamic stiffness accuracy
K	= Stiffness matrix
L	= Cavity width
m	= Rotor mass
M	= Mass matrix
m_R,m_Q	= Direct, cross-coupled inertia of test seal
p	= Pressure distribution along the surface
$\hat{p}$	= Zero-to-peak value of measured pressure oscillation
q	= Displacement vector
$q_{MidNode}$	= Displacements at mid node
q_{sensor}	= Displacements at sensors
r	= Rotor radius at labyrinth position
t	= Time
T_i,T_s	= Corrective transfer functions
U	= Input vector of control currents and labyrinth force
U_{Plant}	= Input vector of plant
w	= Force input vector
$\underline{x}$	= Vectors of measured displacements
x,y	= Displacement in x-, y-direction
x_1,x_2	= Displacement in 1-, 2-direction
Y	= Output vector of displacements at sensors and mid node
Y_{Plant}	= Output vector of plant
β	= Phase between position and pressure signal
φ	= Angle between normal vector of surface and x-axes
ω	= Rotational rotor speed
Ω	= Precession angular frequency
Ω_{rel}	= Angular frequency of shaft surface (= $\omega-\Omega$)
Ω_{wall}	= Angular frequency of stator surface (= $-\Omega$)

REFERENCES

API Standard 617, 2002, "Axial and Centrifugal Compressors and Expander-Compressors for Petroleum, Chemical and Gas Industry Services," Seventh Edition, American Petroleum Institute, Washington, D.C.

Baumann, U., 1999, "Rotordynamic Stability Tests on High-Pressure Radial Compressors," *Proceedings of the Twenty-Eighth Turbomachinery Symposium*, Turbomachinery Laboratory, Texas A&M University, College Station, Texas, pp. 115-122.

Benckert, H., 1980, "Strömungsbedingte Federkennwerte in Labyrinthdichtungen," Dissertation, Universität Stuttgart.

Childs, D. W., 1993, *Turbomachinery Rotordynamics, Phenomena, Modeling & Analysis*, New York, New York: John Wiley & Sons, Inc.

Childs, D. W. and Picardo, A., 2005, "Rotordynamic Coefficients for a Tooth-on-Stator Labyrinth Seal at 70 Bar Supply Pressures: Measurements Versus Theory and Comparisons to a Hole-Pattern Stator Seal," *Journal of Engineering for Gas Turbines and Power*, *127*, pp. 843-855.

Childs, D. W. and Scharrer, J. K., 1986, "Experimental Rotordynamic Coefficient Results for Teeth-on-Rotor and Teeth-on-Stator Labyrinth Gas Seals," ASME-Paper 86-GT-12.

Childs, D. W. and Vance, J. M., 2007, "Annular Gas Seals and Rotordynamics," Short Course 2 held at the Thirty-Sixth Turbomachinery Symposium, Turbomachinery Laboratory, Texas A&M University, College Station, Texas.

Cochrane, W., 1976, "New Generation Compressor Injecting Gas at Ekofisk," *Oil and Gas Journal*, pp. 63-70.

Gupta, K. G., Soulas, T. A., and Childs, D. W., 2007, "New Steps to Improve Rotordynamic Stability Predictions of Centrifugal Compressors," GT2007-27501, ASME Turbo Expo 2007, Montreal, Canada.

Kirk, R. G., 1988, "Evaluation of Aerodynamic Instability Mechanisms for Centrifugal Compressors—Part II: Advanced Analysis," *Journal of Vibration, Acoustics, Stress and Reliability in Design*, *110*, pp. 207-212.

Kocur, J. A., Nicholas, J. C., and Lee, C. C., 2007, "Surveying Tilting Pad Journal Bearing and Gas Labyrinth Seal Coefficients and Their Effect on Rotor Stability," *Proceedings of the 36th Turbomachinery Symposium*, Turbomachinery Laboratory, Texas A&M University, College Station, Texas, pp. 1-10.

König, S., Petry, N., and Wagner, N. G., 2009, "Aeroacoustic Phenomena in High Pressure Centrifugal Compressors—A Possible Root Cause for Impeller Failures," *Proceedings of the Thirty-Eighth Turbomachinery Symposium*, Turbomachinery Laboratory, Texas A&M University, College Station, Texas.

Memmott, E. A., 1999, "Stability Analysis and Testing of a Train of Centrifugal Compressors for High Pressure Gas Injection," *Journal of Engineering for Gas Turbines and Power*, *121*.

Moore, J. J., Ransom, D. L., and Viana, F., 2007, "Rotordynamic Force Prediction of Centrifugal Compressor Impellers Using Computational Fluid Dynamics," GT2007-28181, ASME Turbo Expo 2007, Montreal, Canada.

Schettel, J., Deckner, M., Kwanka, K., Lüneburg, B., and Nordmann, R., 2005, "Rotordynamic Coefficients of Labseals for Turbines—Comparing CFD Results with Experimental Data on a Comb-Grooved Labyrinth," GT2005-68732, ASME Turbo Expo 2005, Reno-Tahoe, Nevada.

Schmied, J., Spirig, M., Wagner, N. G., and Critchley, P., 2002, "Influence of Seals with Frequency Dependent Characteristics on the Rotordynamic Behaviour of High Pressure Compressors," VDI-Conference Fluid-Struktur-Wechselwirkung, Wiesloch, Germany.

Smith, K. J., 1975, "An Operation History of Fractional Frequency Whirl," *Proceedings of the Fourth Turbomachinery Symposium*, Turbomachinery Laboratory, Texas A&M University, College Station, Texas, pp. 115-125.

Wachel, J. C. and von Nimitz, W. W., 1980, "Assuring the Reliability of Offshore Gas Compression Systems," European Offshore Petroleum Conference & Exhibition, London, England.

Wagner, N. G., 2001, "Methode zur Identifikation der dynamischen Labyrinthkoeffizienten für Hochdruckverdichter mit Hilfe aktiver Magnetlager," Dissertation, TU Darmstadt, published as Fortschritt-Berichte VDI, Reihe 11, Nr. 295.

Wagner, N. G. and Steff, K., 1996, "Dynamic Labyrinth Coefficients from a High-Pressure Full-Scale Test Rig Using Magnetic Bearings," Rotordynamic Instability Problems in High-Performance Turbomachinery, NASA Conference Publication 3344, pp. 95-112.

BIBLIOGRAPHY ON CFD-RELATED LITERATURE

Arghir, M., Defaye, C., and Frene, J., 2006, "The Lomakin Effect in Annular Gas Seals under Choked Flow Conditions," ASME Turbo Expo 2006: Power for Land, Sea and Air, Barcelona, Spain.

Athavale, M. M. and Hendricks, R. C., 1996, "A Small Perturbation CFD Method for Calculation of Seal Rotordynamic Coefficients."

Bissig, M. and Staubli, T., 2002, "Numerische Berechnung der Fluid-Rotorinteraktion im Radseitenraum von Hydromaschinen," VDI-Tagung Fluid-Struktur-Wechselwirkung, Heidelberg, Germany.

Geis, T., 2002, "Strömungs und reibungsinduzierte Leistungs- und Wirkungsgradverluste in komplexen Rotor-Stator Zwischenräumen," Dissertation an der Universität Karlsruhe.

Hsu, Y. and Brennen, C. E., 2002, "Effect of Swirl on Rotordynamic Caused by Front Shroud Pump Leakage," *Journal of Fluids Engineering*.

Leeb, K., 1997, "Experimentelle und numerische Untersuchungen zum Durchflußverhalten von Labyrinthdichtungen von Turbomaschinen unter dem Einfluß von Rotation," Wellendesaxierung und Drall der Zuströmung, Dissertation an der Technischen Universität Wien.

Schettel, J. and Nordmann, R., 2004, "Modeling Flow Induced Forces in Turbine Labyrinth Seals," Ecole Polytechnique, Paris, France.

Schettel, J. and Nordmann, R., 2005, "Bestimmung der rotordynamischen Koeffizienten von Labyrinthdichtungen komplexer Geometrien zum Einsatz in Dampfturbinen höchster Wirkungsgrade," AG Turbo II Abschlussbericht.

Spirig, M. and Staubli, T., 1997, "Identification of Non-linear Rotor Dynamic Coefficients Using Multiple Circumferential Pressure Measurements," Zürich, Switzerland.

Xi J. and Rhode, D. L., 2005, "Rotordynamics of Turbine Labyrinth Seals with Rotor Axial Shifting," *International Journal of Rotating Machinery*, *2006*.

ACKNOWLEDGEMENT

The authors thank the management of the Siemens Energy Sector, Oil & Gas Division, for publication permission. The contributions to this project from many persons, all of whom cannot be listed here, are highly appreciated.